Various Types of Defects Detection in Flat and Curved Laminated Composite Plates Using Nonintrusive Lamb Wave System

Lingyu Yu
Department of Mechanical Engineering,
University of South Carolina,
300 Main Street,
Columbia, SC 29208
e-mail: yu3@cec.sc.edu

Zhaoyun Ma[1]
Department of Mechanical Engineering,
University of South Carolina,
300 Main Street,
Columbia, SC 29208
e-mail: zhaoyun@email.sc.edu

Composite materials are widely used in aerospace industries due to their light weight, strength, and various other desired properties. However, they are susceptible to various defects occurring during the manufacturing process or in service. Typical defects include porosity, wrinkles, and delamination. Nondestructive means of detection of the defects at any stage are of great importance to ensure quality and safety of composite structures. A nonintrusive removable Lamb wave system and accompanied methodology that is not material dependent are presented in this paper to detect various types of typical defects in laminated composite plates, flat or curved. Through multidimensional data acquisition and processing, abnormality in waves caused by defects is captured and presented in inspection images. The methodologies are demonstrated in two cases: delamination in a curved plate and wrinkles in a flat plate. Overall, the results show that Lamb waves using the piezoelectric transducer and laser vibrometer system can be used for various types of defects inspection in flat or curved composite plates. [DOI: 10.1115/1.4049468]

Keywords: composite structures, delamination, curvature, wrinkles, Lamb waves, laser vibrometer

1 Introduction

Composite materials are widely used in aerospace and aeronautical industries, and the interest in using more advanced composites is growing high [1] because of their advantages for lightweight, high strength, and engineering design flexibility. The large use of composites necessitates the development of appropriate nondestructive evaluation (NDE) methods to detect and quantify defects and damage in composites [2–4]. The National Aeronautics and Space Administration (NASA) Aeronautics Research Mission Directorate initiated research to reduce the certification time of composite components under the Advanced Composites Project [4,5] with one of the three technical challenges being developing NDE methods to quantitatively characterize defects in as-manufactured parts and damage incurred during or after manufacturing [2]. Various defects such as fiber waviness or undesirable material may appear in composite structures during the manufacturing process [6]. Wrinkles or waviness are common when adding new layers [7] or during curing with temperature gradients [2]. Wrinkles/waviness can be in-plane or out-of-plane [8] and will cause significant degradation of the composite strength and can weaken the composite structure performance. Debonding occurs when an adhesive stop adhering to an adherend or if physical or mechanical forces that hold the bond together are broken while delamination is a failure in a laminate which leads to separation of the layers or plies. All these undesirable defects affect the mechanical properties and structural overall performance [6], and may further jeopardize the safety of space structures during operation. Thus, nondestructive evaluation methods that are suitable for a wide range of defects are highly needed [1,9] for ensuring safety and reliability of aeronautic vehicles [5,10].

Lamb waves can propagate relatively long distances in plate-like structures with lower energy loss compared to bulk waves, which enables their ability for large area inspection [11,12], and they are sensitive to various defects [13,14]. With these advantages, Lamb wave-based NDE methods have been widely applied for defect detection in plate-like composite structures over the last decade [15–19]. Park et al. adopted time-reversal algorithms to reconstruct the Lamb waves excited by a piezoelectric patch in a quasi-isotropic composite plate toward a reference-free diagnosis technique [15]. Purekar and Pines used piezoelectric sensor (PZT) arrays to excite and receive Lamb waves for damage detection purposes in a composite plate with simulated delamination [16]. Rogge and Leckey demonstrated Lamb wavefield analysis and wavenumber imaging can be used to identify the depth and size of near-surface impact delamination in composite plates [17]. Hall and Michaels studied the multipath-guided wave imaging method using sparser arrays on a composite plate with simulated damage, resulting in improved image quality compared to their previous work [18]. Sohn et al. applied a filtering imaging method and highlighted the internal delamination using standing waves trapped within a composite plate [19]. Tian et al. quantified impact delamination dimensions in composite plates through wavenumber-based imaging methods [20].

Recently, the scanning laser Doppler vibrometer (SLDV) has attracted great interest in Lamb wave-based defect detection, visualization, and quantification [14,21–26]. Based on the Doppler effect, the SLDV can acquire velocities/displacements of Lamb waves on the plate surface where the laser inspection spot aims at. By scanning over a high-density set of points over the wave propagation area, the SLDV can acquire a high-resolution wavefield, which contains a wealth of information about the Lamb wave propagation and interactions with a defect in plates. Such high-resolution wavefields have been used for visualization and quantification of various types of defects, such as cracks, delamination, and debonding [27–31]. However, most of the work reported in the literature for Lamb wave-based defect detection in
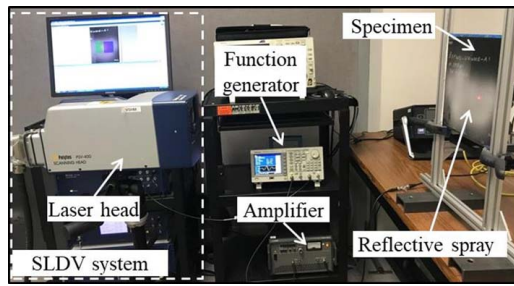
Fig. 1 Experimental setup of the nonintrusive PZT-SLDV system

composites is mainly about delamination on flat plates or slightly curved ones [14,17,20].

This paper investigates the detection and evaluation of wrinkles and delamination defects in either flat or curved laminated composite plates using PZT-SLDV Lamb waves and multidimensional wavefield analysis. Laboratory experiments are first set up to provide minimally invasion to the plates being inspected, and the Lamb wave wavefields are obtained. For defect visualization and evaluation, two methods, adaptive wavefield imaging and wavenumber imaging, are developed and applied for the flat and curved plate scenarios, respectively. The inspection results show that the imaging methods can not only visually show the location of the defects but also roughly quantify their sizes. The remainder of this paper is organized as follows: Sec. 2 presents the nonintrusive PZT-SLDV inspection experimental setup. Section 3 presents the visualization and localization of delamination in a curved plate, while Sec. 4 presents that of wrinkle defects in a flat composite plate. Section 5 then concludes the paper with findings, discussions, and future work.

2 Nonintrusive Piezoelectric-Scanning Laser Doppler Velocimetry Lamb Wave System Setup

This section presents the nonintrusive experimental setup of the PZT-SLDV Lamb wave inspection system. The overall experimental setup of the PZT-SLDV system is given in Fig. 1. A Steminc SM412[2] PZT transducer (0.5 mm thick and 7 mm diameter) is used for Lamb wave actuation, while the Polytech PSV-400-M2 SLDV system is employed for wavefield sensing. Traditionally, the PZT transducer is bonded on the surface with permanent adhesive as couplant, while reflective tapes are attached on the specimen surface for SLDV signal enhancement [23]. Removing the PZT transducer or the reflective tape requires great care and may more or less still cause adverse modification of the material surface conditions. In order to implement truly nondestructive evaluation on the composite structures, nonintrusive setup is explored and implemented in this study, with selected honey (Fig. 2(a)) as couplant for PZT actuation and wipe-off reflective spray (Fig. 2(b)) for SLDV measurement enhancement.

To attach the PZT transducer, a syringe is used to apply a tiny drop of honey at the target surface and the PZT is then placed on top of the honey drop. Gentle thumb pressure is applied on the PZT transducer for about two minutes so that the honey will distribute evenly between PZT and the specimen. The attached PZT is then left for a couple of hours before the inspection so that the honey will harden and cure. Figure 2(c) illustrates the PZT transducer attached to the surface with honey. Removable transparent tape is used to hold the wire in place on the plate (as shown in Fig. 2(c)) to help the PZT stay on without sliding down if the specimen is placed vertically. On the other hand, the wipe-off reflective spray is applied with the

spray nozzle being held 12 in. away and normal to the specimen surface as shown in Fig. 2(d). About 20 layers of spray are applied to the surface in order to achieve full signal level from the SLDV.

For Lamb wave inspection, three-count Hanning window smoothed sinusoidally is used as excitation. It is generated by a function generator (Tektronix AFG3022C) at a selected frequency, magnified by an amplifier (NF HSA 4014) (40 times gain in this study), and then sent to the PZT actuator. Through in-plane piezoelectric coupling [11], Lamb waves are excited and propagate in the plates. On the sensing side, SLDV works on the Doppler frequency-shift effect on light waves and measures particle velocity along its laser beam. For Lamb wave measurements, the SLDV head is placed normal to the specimen to obtain the out-of-plane Lamb wave velocity at a sensing point. In addition, the SLDV head is set up at the optimal standoff distance (506 mm, 711 mm, and 915 mm) to the specimen (711 mm in this study), With its scanning capability, SLDV will obtain the motions over a user-defined scanning line or area grids and output the multidimensional time-space Lamb wavefield $v(t,\mathbf{x})$, where t is the time and $\mathbf{x}$ is the space vector (x,y) of the scanning point. More details of SLDV wavefield sensing can be found in Ref. [20].

3 Delamination Inspection on a Curved Plate

This section presents the inspection of the curved specimen with delamination. To evaluate if the curved specimen can be inspected the same way as a flat one for damage detection purpose, the curved plate is treated as flat during the inspection using the nonintrusive PZT-SLDV inspection system. Studies have shown that when there is delamination in laminated composites, strong trapped waves with new wavenumbers associated with the ply location of the delamination are present and reflected back and forth inside the delamination area [20]. Wavenumber imaging method has been proved effective for delamination detection and quantification in flat or slightly curved composites [14,17,20]. Using the current PZT-SLDV system, the SLDV measurement will be the projection of the actual wavefield due to the curvature of the plate and thus will affect the wavenumber component as well as its strength. In this study, we explored the possibility of using the wavenumber imaging method using the current setup for delamination evaluation on the curved specimen without considering the curvature effect on wavenumbers. The wavenumber imaging algorithms and the inspection results are presented in this section.

### 3.1 Evaluation Method: Weighted Wavenumber Imaging.
Using multidimensional Fourier transform (FT) [32], the SLDV acquired time-space wavefield $v(t, \mathbf{x})$ can be converted to frequency–wavenumber representation to reveal intrinsic wave characteristics related to the propagation and wave–defect interactions [22,32]. Mode conversion and/or new wavenumbers might be introduced due to the defect and further modify the distribution of the wavenumbers, which presents how the Lamb waves are modified at defect due to the wave-defect interactions. Hence, a wavenumber distribution map can be used to directly indicate the presence of the defect as well as its location in the structure.

In this study, a weighted wavenumber imaging method [33] using wavenumber information at selected frequencies of interest is developed and applied for the delamination detection in the curved plate. The method first transfers the acquired time-space wavefield $v(t, \mathbf{x})$ to the frequency-space representation $V(f, \mathbf{x})$ through 1D Fourier transform with respect to time t, given as

$$V(f, \mathbf{x}) = \int_{-\infty}^{\infty} v(t, \mathbf{x})e^{-j2\pi ft}dt \qquad (1)$$

After that, short-space two-dimensional (2D) FT previously developed in Ref. [20] is applied to the frequency-space wavefield
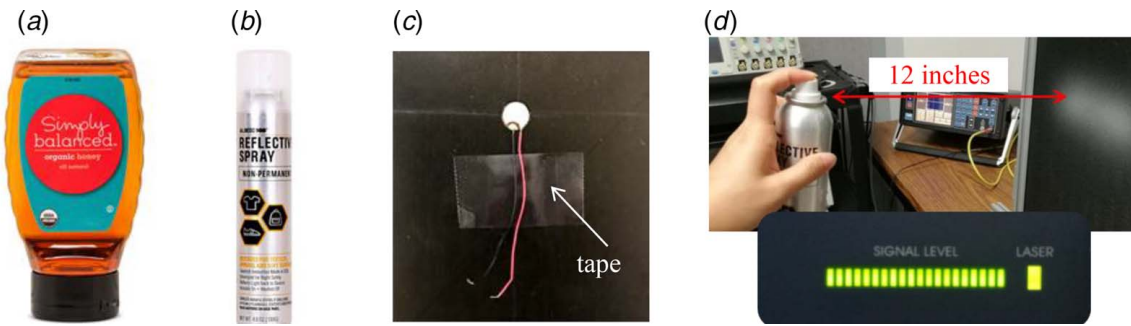
Fig. 2 Nonintrusive PZT-SLDV system setup: (a) honey couplant by simply balanced, (b) wipe-off reflective spray by Albedo 100, (c) PZT attached using honey as couplant. Transparent tape is used to hold the wire in place on the plate and (d) spray applying illustration and related signal strength.

$V(f, \mathbf{x})$ with respect time-space $\mathbf{x}$, resulting in a space-frequency–wavenumber representation $S(\bar{\mathbf{x}}, f, \mathbf{k})$, as

$$S(\bar{\mathbf{x}}, f, \mathbf{k}) = \int_{-\infty}^{\infty} \int_{-\infty}^{\infty} V(f, \mathbf{x}) W(\mathbf{x} - \bar{\mathbf{x}}) e^{j\mathbf{k} \cdot \mathbf{x}} d\mathbf{x} \quad (2)$$

where $\bar{\mathbf{x}}$ is the retained spatial vector $(\bar{x}, \bar{y})$ for each scanning point, $\mathbf{k}$ is the counterpart of $\mathbf{x}$ in the wavenumber domain, and $W(\mathbf{x})$ is a spatial window function centered at $\bar{\mathbf{x}}$ sliding through the whole scanning area during the process of short-space 2D FT. In this study, Hanning window is used [34], given as:

$$W(\mathbf{x}) = \begin{cases} \dfrac{1}{2} \left[1 + \cos\left(2\pi \dfrac{|\mathbf{x}|}{D}\right) \right] & \text{if } |\mathbf{x}| \leq D/2 \\ 0 & \text{otherwise} \end{cases} \quad (3)$$

where D is the window width in the space domain along both x and y directions. More details of the short-space 2D FT can be referred to Ref. [20]. In order to obtain the dominant wavenumber distribution in the scanned area, the calculated $S(\bar{\mathbf{x}}, f, \mathbf{k})$ at each scanning point $\bar{\mathbf{x}}$ is weighted by considering the contribution of each wavenumber component $|\mathbf{k}|$, resulting in a dominant wavenumber function $k(\bar{\mathbf{x}}, f)$ [33], which is expressed as

$$k(\bar{\mathbf{x}}, f) = \frac{\sum_{k} |S(\bar{\mathbf{x}}, f, \mathbf{k})| |\mathbf{k}|}{\sum_{k} |S(\bar{\mathbf{x}}, f, \mathbf{k})|} \quad (4)$$

The obtained wavenumber function $k(\bar{\mathbf{x}}, f)$ represents a weighted wavenumber distribution within an area defined by $\bar{\mathbf{x}}$ at each frequency f. Note, this wavenumber function is only used for damage detection purposes and cannot represent the actual

wavenumber distribution in the plate since all the modes are considered. To acquire the wavenumber image at the excitation frequency with a good resolution, an image fusion technique is performed by taking the average of $k(\bar{\mathbf{x}}, f)$ over a selected frequency range about the excitation frequency, expressed as

$$k(\bar{\mathbf{x}}) = \frac{1}{N} \sum_{i=1}^{N} k(\bar{\mathbf{x}}, f_i) \quad (5)$$

where f_i $(i = 1, 2, 3 \dots N)$ are the frequencies within the selected frequency band. Therefore, $k(\bar{\mathbf{x}})$ in Eq. (5) is the weighted wavenumber distribution plotted as an intensity image that shows how the dominant wavenumber changes at defect when it is present.

3.2 Evaluation of Delamination in the Curved Plate. The curved composite plate is manufactured with embedded delamination between different layers. The top surface and side view of the curved plate are shown in Figs. 3(a) and 3(b), respectively. The plate measures about 101 mm high and 7 mm thick, and 160-mm top surface arc length. Two area inspections are performed on the plate with one for wing W1 and another for W2 as shown in Fig. 3(c). A three-count toneburst amplified to 40 Vpp is used as excitation for each inspection. The excitations are located at the center of each wing O_1 (40 mm away from the left edge and 50 mm away from the bottom edge) for W1 and O_2 (40 mm away from the right edge and 50 mm away from the bottom edge) for W2, so that the wave propagation can cover the entire wing. Considering that the measurement on different surfaces may vary due to the nonsymmetric defect location across the thickness/layer with respect to each surface for composite plates [20], the measurement has been conducted on both the top and bottom surfaces. The
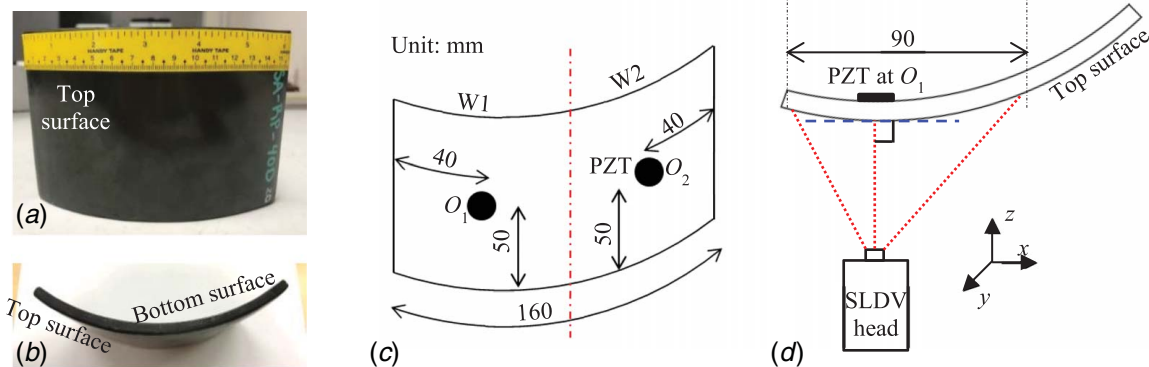
Fig. 3 Inspection of the curved plate with delamination (photo courtesy of NASA Langley Research Center and the advanced composites consortium (ACC) members): (a) top surface view, (b) side view showing the curvature, (c) actuation locations for W1 and W2 inspection, and (d) actuation and sensing schematic for W1

inspection frequency is set as 150 kHz as it provides strong wave–defect interaction. The SLDV head is placed normal to the surface where the excitation is located as shown in Fig. 3(*d*). Due to the curvature of the plate, the SLDV will not maintain normal to the plate surface of the whole scan area, as illustrated in Fig. 3(*d*). Such scanning angle effect and resulted loss in wave strength are not considered in this study since our study goal is to explore if the present measurement and analysis methods are applicable for delamination detection on plates with such amount of curvature. For each inspection, the scanning area covers the accessible surface of the inspected wing: around 90 mm × 90 mm within *x*–*y* plane. The SLDV spatial resolution is 1 mm, and the sampling rate is 10.24 MHz. Note the inspection area on the top and bottom surface differs subtlety due to the plate curvature.

Figures 4(*a*) and 4(*b*) plot the wavefield snapshots at 45 μs for W1 and W2 inspection on the top surface. The wave–delamination interactions can be immediately noticed at two locations along *y* = 50 mm (marked as D2) and 82 mm (marked as D1) from the wavefield plots. Similar wave–defect interactions are observed: (a) defect-induced waves at D1 as shown in Fig. 5(*d*) with significantly smaller wavelength compared to the 10-mm nominal wavelength of the incident waves (Fig. 4(*c*)); (b) defect-induced waves at D2 (Fig. 4(*e*)) with obvious higher intensity while no obvious wavelength change compared to the incident waves (Fig. 4(*e*)), indicating the possibility of the presence of a defect.

Further evaluation of the delamination in the curved plate is conducted with the weighted wavenumber imaging method given in Sec. 4.1. The resulted wavenumber images are plotted in Figs. 5(*a*) and 5(*b*). From the image for W1 (Fig. 5(*c*)), a strip-shaped defect (D1) is highlighted with large wavenumbers in the range 40 mm to 90 mm along *y* = 82 mm, which is consistent with the shorter wavelength observed in the wavefield snapshot (Fig. 4(*d*)) given the inverse relationship between wavenumber and wavelength [20]. In addition, another strip-like defect (D2) can also be observed in the range *x* = 40–90 mm at *y* = 50 mm through the indication via slightly wavenumber variations, which is consistent with the wavefield observation that no obvious wavelength changes (Fig. 4(*e*)). In the wavenumber image for W2 (Fig. 5(*b*)), D1 (*y* = 80 mm) and D2 (*y* = 50 mm) are indicated in the range 60–110 mm along *x*-axis. By comparing the imaging results of W1 and W2, we can conclude that D1 and D2 are localized in the range 40–110 mm along *x*-axis with D1 at 82 mm and D2 at 50 mm along *y*-axis.
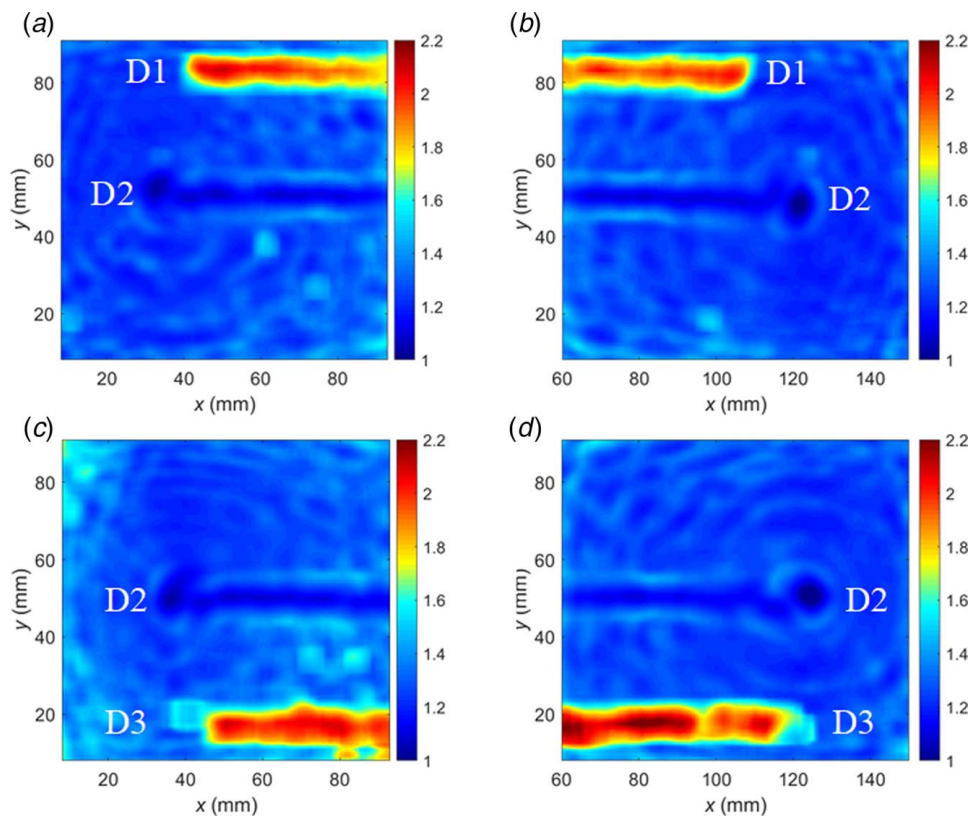
The inspection wavenumber imaging results obtained on the bottom surface are presented in Figs. 5(*c*) and 5(*d*). Similar subtle wavenumber variations are observed at the D2 location detected earlier on the top surface, which further confirms the D2 range and shape. In addition, another strip-shaped defect (D3) is observed, located at *y* = 18 mm with a similar range along *x*-axis, 40–110 mm by considering the results of both Figs. 5(*c*) and 5(*d*). Through comparing the inspection results on the top and bottom surfaces, we can conclude that (1) three strip shape defect exists in the plate in the range of 40–110 mm along the *x*-axis with D1 at 82 mm, D2 at 50 mm, and D3 at 18 mm along *y*-axis, and (2) along the thickness direction, D1 is close to top surface since it is only clearly highlighted in the results obtained on the top surface, while D3 is close to the bottom surface since it is only visualized in the results measured on the bottom surface. D2 shall be located within the middle plane since the interaction is more difficult to capture on both surfaces resulting in lower imaging resolution.

4 Wrinkles Inspection on a Flat Plate

In this section, out-of-plane wrinkle defects are evaluated in a flat laminated composite plate. A simulation study has shown that wavenumber-based methods are not sensitive to wrinkle defects since no new wavenumbers are introduced, while the first arrival (S0) shows sensitivity to wrinkles [2,3]. Wavefield imaging method based on the first arrival has been used by Michaels [35] for bond quality detection in a bonded aluminum plate since S0 is almost non-dispersive in the low-frequency-thickness range [36,37], and it is not complicated by the slower modes and edge reflections [35]. The imaging results in Michaels' study are significantly improved compared to the wavefield imaging method using the whole wave signal. Within the acquired multidimensional time-space wavefield in this study, strong interactions between the wrinkle and the first arrival are observed. Hence, an adaptive wavefield imaging method has been developed using the time of flight information of the first arrival in the acquired waves and applied to evaluate the wrinkle defect. The adaptive wavefield imaging algorithms and the inspection results are presented in this section.
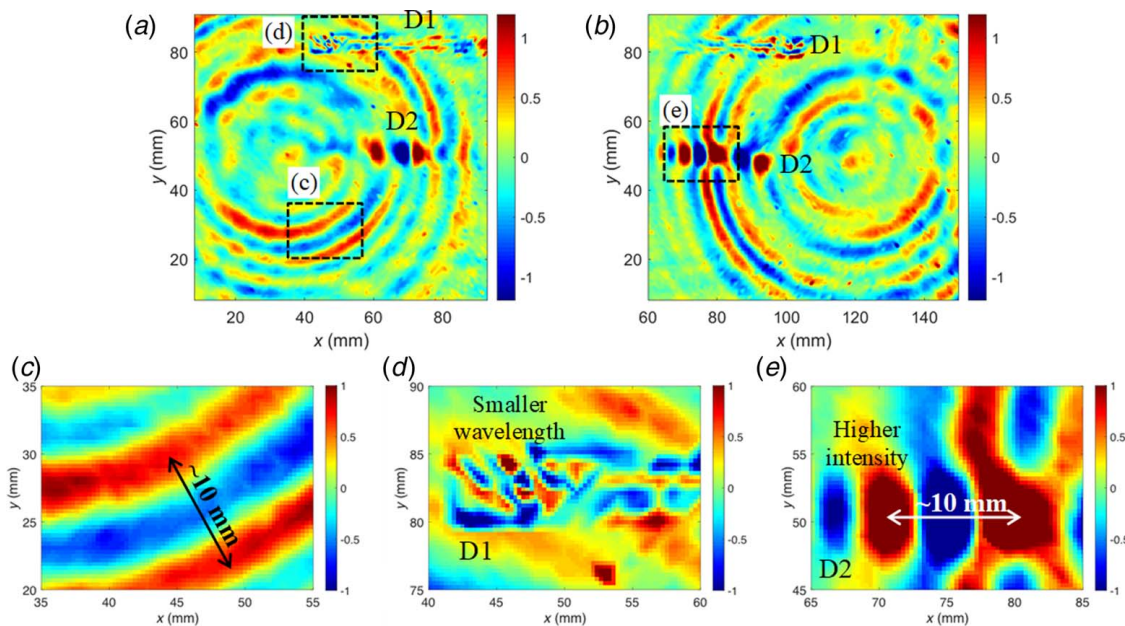
Fig. 4 Wavefield result at 45 μs obtained on the top surface of (*a*) W1, (*b*) W2, (*c*) zoom-in view of the wavelength of incident waves, (*d*) zoom-in view of the smaller wavelength of the defect-induced waves, and (*e*) zoom-in view of the larger wavelength of the defect-induced waves

Fig. 5 Wavenumber imaging results of the curved plate obtained on the top surface: (*a*) W1 and (*b*) W2, obtained on the bottom surface: (*c*) W1 and (*d*) W2

4.1 Evaluation Method: Adaptive Wavefield Imaging. Very often, directly acquired wavefield does immediately show the wave–defect interactions, indicating the existence of structural discontinuity [19,20,31,33]. However, such detection requires experiences of wavefield analysis, and immediate visualization of discontinuity in the structure is highly desired. Studies have shown that evaluating the wave energy along the wave propagating distance provides a rapid yet effective way to generate an inspection image of the plate [38,39]. The wave energy can be represented by quantities such as the peak amplitude or the root-mean-square value of the waveform at the position [35]. However, it has shown that the resolution of such images are limited and the revealed defect features are not clear enough for quantification purpose [35].

Due to the multimodal property of Lamb wave [36], there are always at least two modes existing in the propagation. They usually travel at largely different velocities, resulting in a faster wave packet arriving first than other slower ones. The first arrival will yield clearer interaction features since it is less likely complicated by the slower modes or boundary reflections [35]. In this research, an adaptive wavefield imaging method has been developed that employs the first arrival for the evaluation of wrinkle defects in the flat composite panel. Assume the group velocity c_g of such a first arrival is known, its time of flight at a point (x,y) of interest in the plate can be determined as

$$t_{tof}(\mathbf{x}) = \frac{\left|\sqrt{(x-x_0)^2 + (y-y_0)^2}\right|}{c_g} \qquad (6)$$

where (x_0, y_0) is the location of the excitation source. Using the calculated $t_{tof}(\mathbf{x})$, the first arrival of the acquired wave can be retained through a windowing technique. The window $W_{t_{tof}}(t)$ is defined with its center at $t_{tof}(\mathbf{x})$ and having a width of the double

length of the excitation signal. The window is then applied to the wavefield as

$$v_{1st}(t, \mathbf{x}) = v(t, \mathbf{x})W_{tof}(t) \qquad (7)$$

In our work, a Tukey window [40] is used since it offers a "flat-top" to have unit gain within the interesting time frame of first arrival signals. Using the windowed first arrival, an intensity image based on the amplitude information is then generated to indicate the presence of the defect as well as its locations

$$v_{1st}^{mag}(t, \mathbf{x}) = \max |v_{1st}(t, \mathbf{x})| \qquad (8)$$

4.2 Evaluation of Wrinkle Defect. The flat composite plate is manufactured with a total of 20 plies and 3.83 mm thickness. The overall dimension of the plate is measured at 306×260 (unit: mm). Significant wrinkles can be observed on both top and bottom surfaces, as illustrated in Fig. 6(*a*) (indicated by the arrows), and also can be seen from the side along the thickness direction as in Fig. 6(*b*). No other information about this wrinkle plate is available such as the material properties as well as the detailed layup. To assist the inspection, Cartesian coordinates are employed with the origin set at the left bottom corner of the plate. We have chosen to study the area with more visible wrinkles and referred to it as "wrinkle region," in contrast to the area with less visible wrinkles as "reference region," as shown in Fig. 6(*c*). A PZT actuator is placed at location (160, 110) on the specimen (Fig. 6(*c*)) to excite the waves. The actuator is about 30 mm away from the wrinkle edge as shown in Fig. 6(*b*), which is far away enough from the wrinkle edge so that the "blind zone" near the source is avoided and it allows the two modes to separate when they arrive at the wrinkles. Area scans (95 mm by 60 mm in the range $x = 60–160$ mm and $y = 80–140$ mm) are performed using the area scan setup given in Fig. 6(*c*). Similar to Sec. 3, the measurement
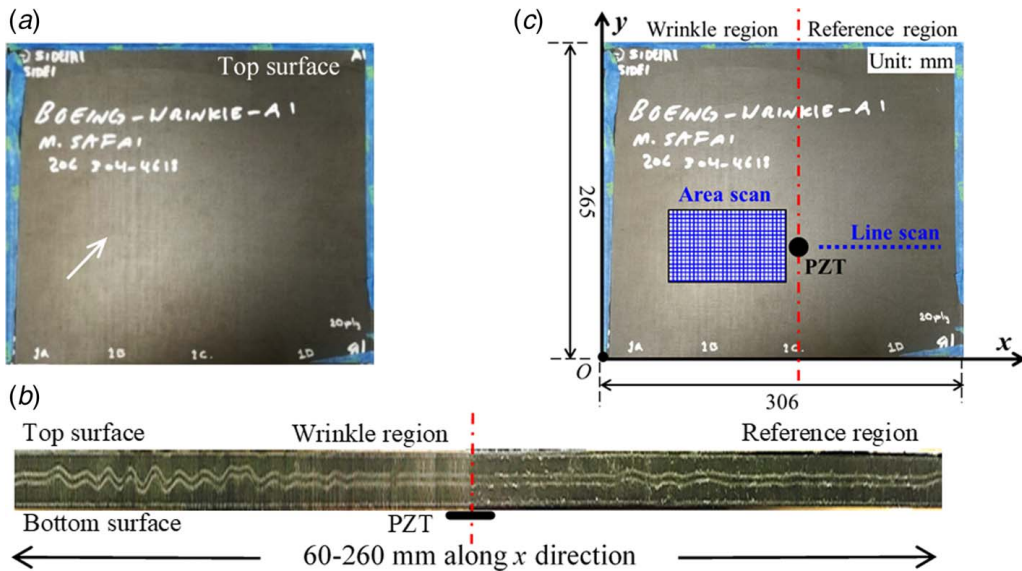
Fig. 6 Inspection of the composite plate with wrinkle defect (photo courtesy of NASA Langley Research Center and Boeing): (*a*) top surface, (*b*) side view, and (*c*) actuation and sensing schematic
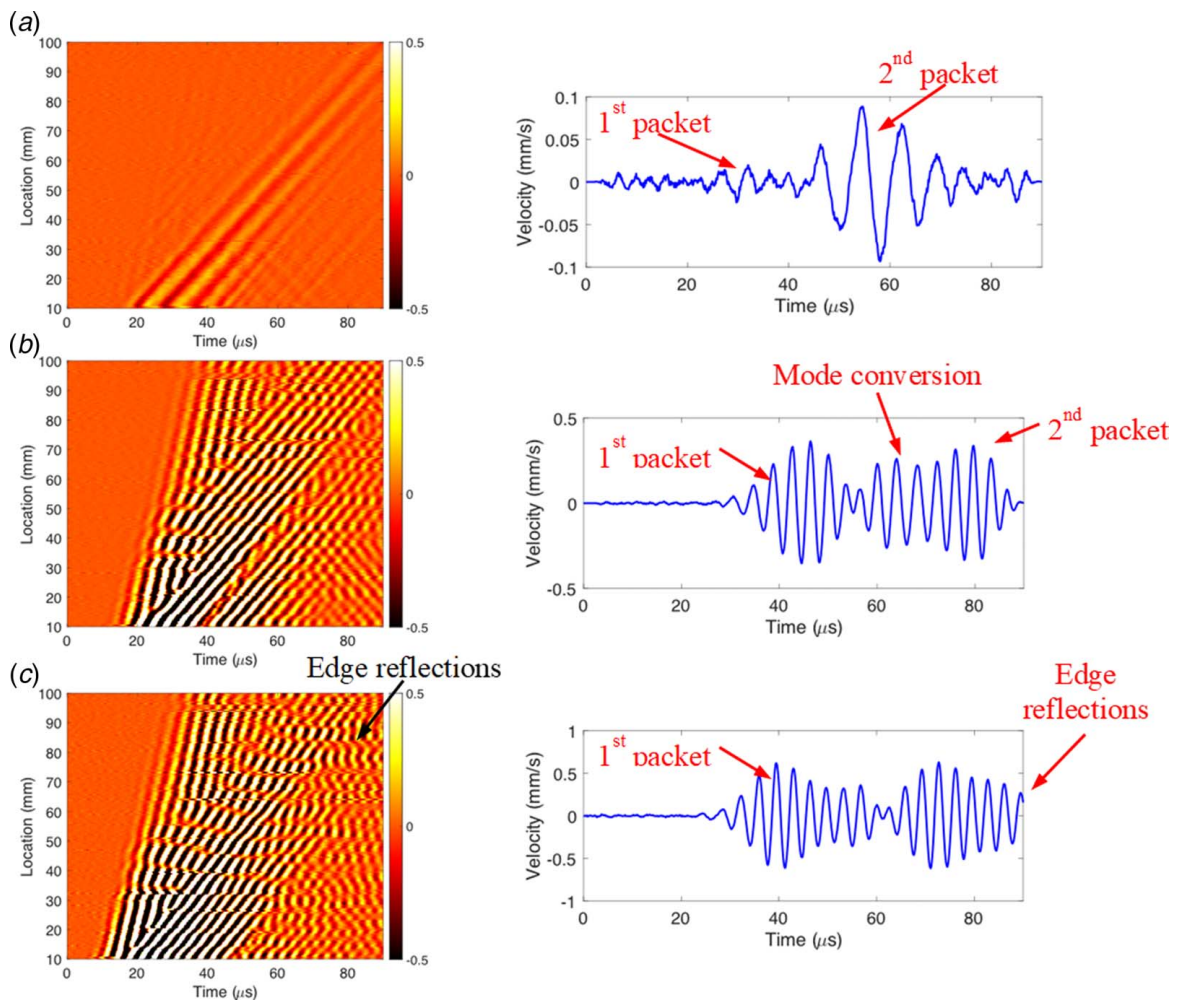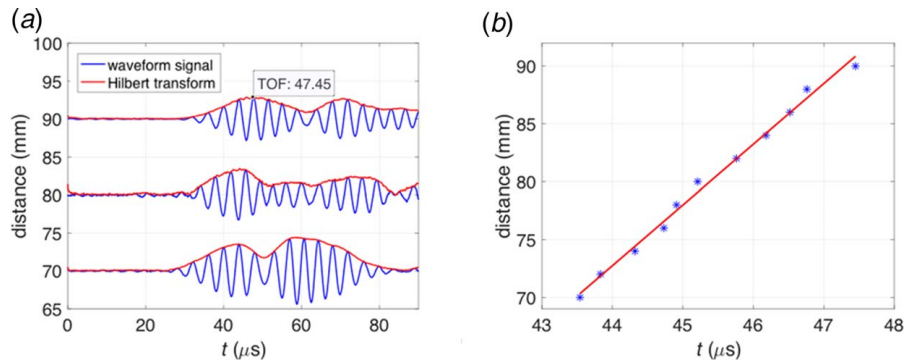

Fig. 7 Line inspection results: (*a*) time-space wavefield at 120 kHz and representative waveform at 50 mm, (*b*) time-space wavefield at 210 kHz, and representative waveform at 85 mm, and (*c*) time-space wavefield at 300 kHz, and representative waveform at 85 mm

Fig. 8 Group velocity estimation of the first arrival: (a) waterfall plots of representative waveforms (at propagating distance 70, 80, and 90 mm) that are used for the group velocity estimation, and (b) more accurate group velocity estimated by the slope of linear regression results

has been conducted on both the top and bottom surfaces in the wrinkle region. A line scan within the reference area has also been performed for inspection parameter setup. The SLDV scanning spatial resolution is 1 mm, and the sampling rate is 10.24 MHz.

For Lamb waves NDE, as frequencies go higher, more wave modes are likely to be excited and cause complexity in subsequent damage evaluation. Therefore, low frequency is often employed [41]. A few quick wave acquisitions at different excitation frequencies through line scans (Fig. 6(c)) are first performed in the reference region to identify a proper excitation frequency. The scans are along x-axis from 10 to 100 mm away from the PZT actuator. The representative acquired time-space wavefield at 120 kHz, 210 kHz, and 300 kHz as well as a waveform at a certain propagating distance is presented in Fig. 7. From Fig. 7(a), we can see that there are two wave packets (S0 and A0) in the 120-kHz Lamb waves but the first arrival (S0) at about 30 μs has very weak strength. And in the wavefield, we can barely observe any wave–wrinkle interactions. On the other side, the first arrival (S0) of the waves at 210 kHz in Fig. 7(b) exhibits much stronger strength. And more obvious wave–wrinkle interactions (S0 to A0 mode conversion) can be observed in the wavefield, indicating that S0 is more sensitive to the wrinkle defect than A0. When the excitation goes up to 300 kHz, the two modes are more difficult to separate and more edge reflections can be observed as shown in Fig. 7(c) due to its faster group velocity. By comparing the results in Fig. 7, 210 kHz will be ideal for the wrinkle inspection since sufficient first arrival will be excited and less complexity will be introduced. Thus, 210 kHz will be used as the excitation frequency for the inspection of the wrinkle plates.

To implement the imaging algorithm, the group velocity of the first arrival in the acquired waves at 210 kHz needs to be determined by finding out its time of flight (TOF) at a given propagation distance. To estimate the group velocity more accurately, eleven

signals from 70 to 90 mm at a 2-mm increment along the scanning line are used. Three example waveforms at propagating distance 70, 80, and 90 mm are plotted in Fig. 8(a). Hilbert transform is applied to extract the envelopes of these waveforms, and the TOFs of the first arrivals are extracted indicated by the peak arrival time (e.g., TOF is 47.5 μs at 90 mm in Fig. 8(a)). All of the acquired TOF and corresponding propagating distance are plotted in Fig. 8(b) (stars). The plot shows a linear relationship that can be curved fitted through linear regression (red line, derived with linear curve fitting as $y = 5.249x - 158.23$). The group velocity of the first arrival is therefore obtained, which is about 5.249 mm/μs.

Inspection using the subject PZT-SLDV system is performed on the wrinkle region on both top and bottom surfaces of the test plate using the setup given in Fig. 6(c). The resulted time-space wavefield snapshots at 25 μs are presented in Fig. 9. Circular wavefront can be observed in the incident waves leaving the PZT actuator for both results. If there is no defect, the circular waves are expected to propagate and attenuate with propagating distance with no abrupt change [20]. However, in the wavefields, the circular wavefronts are guided and modified due to the wrinkle geometry (with the shape straight and vertical along y-direction) to straight crest ones when they arrived at and passed through the wrinkles [42,43]. These straight crest waves are most likely standing waves formed at the wrinkle area due to the reflections back and forth between the wrinkles. Comparing the waves measured on the top (Fig. 9(a)) and bottom (Fig. 9(a)), the wave interaction with defects are occurring in a similar range (90–130 mm along x-direction). It matches with the visually observed wrinkle range in the plate. The detection of wrinkles from both top and bottom indicates the wrinkles might be manufactured through the thickness and can be inspected from either side.

The wavefield data have been further processed with the adaptive wavefield imaging method outlined in Sec. 3.1, and the results are given in Figs. 10(a) and 10(c) for top and bottom surfaces,
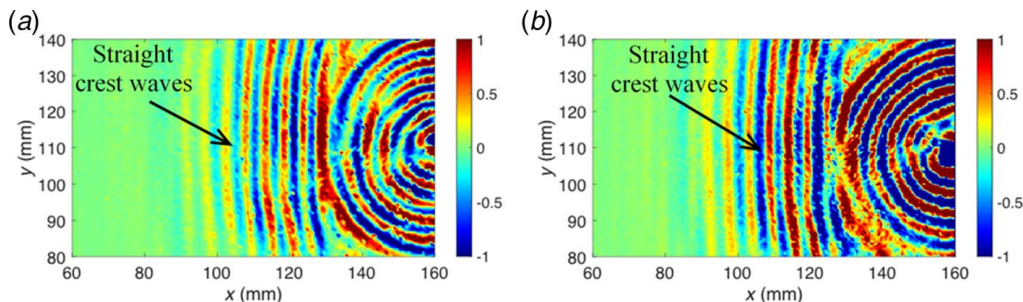
Fig. 9 Wavefield results at 29 μs of the wrinkle region measured on (a) top surface and (b) bottom surface, both showing incident circular crest waves change to straight crest waves
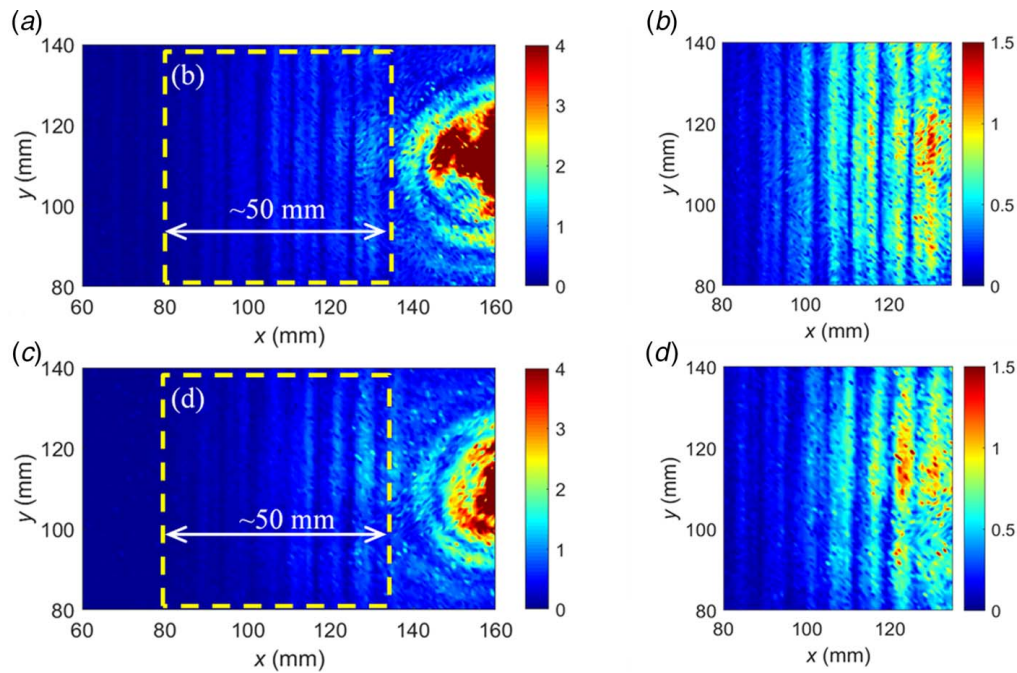
Fig. 10 Wrinkle defect evaluation using adaptive wavefield imaging method. Images obtained on (a) top surface and (c) bottom surface. Zoom-in images of the wrinkle defects on (b) top surface and (d) bottom surface.

respectively. Typically, for the wavefield image generated for a pristine plate, the energy concentrates at the source as shown in Fig. 10 and then gradually decreases with the distance [44]. However, it can be observed in the resulted images that the wave energy has two distinguished distributions in the range 80–130 mm and 130–160 mm. In the range 130–160 mm, the strong energy from the incident waves is observed with a circular shape. While in the range 80–130 mm, strip-shaped wave energy distribution is observed. The zoom-in images of the wrinkle range are presented in Figs. 10(b) and 10(d) for top and bottom surfaces, respectively. Clear wrinkle patterns are visualized now with peaks and valleys represented by the bright and dark colors in both images. The wrinkle patterns are discernibly visualized in both images within the range 80–130 mm along x direction, and the identified wrinkle ranges agree well with that observed through visual examination given in Fig. 6(b).

5 Conclusions

In this paper, two types of composite defects, delamination in a curve plate and wrinkles in a flat plate, are evaluated using a nonintrusive PZT-SLDV system without detailed manufacturing information about the structures. For the evaluation of delamination in the curved plate, promising results are obtained with the current setup. Wavelength change is observed compared to the incident waves in the time-space wavefield, indicating wavenumber changes in the wavenumber domain. The wavenumber imaging method is therefore employed to evaluate the delamination in the curved plate. The resulted images indicate three delamination defects, including their location, overall sizes, and shapes. In addition, the defect location along the thickness direction is indicated with D1 near the top surface, D2 in the middle, and D3 close to the bottom surface. While for the wrinkle plate, the first arrival of the waves shows clear wave interactions with the defect and thus is used to evaluate the wrinkles through an adaptive wavefield imaging method. The resulted images clearly present straight wave patterns caused by the wrinkle defect as well as their location and ranges.

Although both the delamination and wrinkles in the two plates are localized in the resulted images, still some improvements can be achieved for both plates: (1) delamination D2 is not visualized as

clearly as the other two delaminations, and one possible reason could be that the selected excitation location is too close to the defect and (2) the left edge of the wrinkle region on the wrinkle plate is not identified since most of the wave energy scattered after interacting with wrinkles as well as attenuated after propagating long distance. Future work can be focused on trying additional actuator locations such as left and right edges of the plate to cover more inspection views and/or allow wave propagation before the defect or use multiple actuator arrays to excite stronger waves. In addition, the window size effect as well as image fusion can be studied to further improve the wavenumber image resolution. Moreover, comparison with other imaging methods such as ultrasonic C-scan and further implementation of the PZT-SLDV system on other composite defect evaluation such as porosity is also of the authors' interest.

References

[1] Garnier, C., Pastor, M.-L., Eyma, F., and Lorrain, B., 2011, "The Detection of Aeronautical Defects In situ on Composite Structures Using Non Destructive Testing," Compos. Struct., **93**(5), pp. 1328–1336.
[2] Leckey, C. A., and Juarez, P. D., 2016, "Ultrasonic NDE Simulation for Composite Manufacturing Defects," Proceedings of the American Society for Composites 31st Technical Conference, Williamsburg, VA, Sept. 19–22.
[3] Leckey, C. A., and Juarez, P. D., 2016, "Simulation of Guided Wave Interaction With In-plane Fiber Waviness," 43rd Annual Review of Progress in Quantitative Nondestructive Evaluation, Atlanta, GA, July 17–22, p. 020023.
[4] Howell, P. A., 2020, Nondestructive Evaluation (NDE) Methods and Capabilities Handbook-Volume II Appendices: Appendix A–Appendix D.
[5] Leckey, C. A., Seebo, J. P., and Juarez, P., "Challenges of NDE Simulation Tool Validation, Optimization, and Utilization for Composites," Proceedings of AIP Conference. AIP Publishing, p. 120011.

[6] Bowkett, M., and Thanapalan, K., 2017, "Damage Detection and Critical Failure Prevention of Composites," *Failure Analysis and Prevention*, IntechOpen, London, UK.

[7] Radzieński, M., Kudela, P., Marzani, A., De Marchi, L., and Ostachowicz, W., 2019, "Damage Identification in Various Types of Composite Plates Using Guided Waves Excited by a Piezoelectric Transducer and Measured by a Laser Vibrometer," Sensors, **19**(9), p. 1958.

[8] Mizukami, K., Mizutani, Y., Todoroki, A., and Suzuki, Y., 2016, "Detection of In-plane and Out-of-Plane Fiber Waviness in Unidirectional Carbon Fiber Reinforced Composites Using Eddy Current Testing," Compos. Part B: Eng., **86**, pp. 84–94.

[9] Cramer, K. E., Leckey, C. A., Howell, P. A., Johnston, P. H., Burke, E. R., Zalameda, J. N., Winfree, W. P., and Seebo, J. P., 2015, "Quantitative NDE of Composite Structures at NASA," American Society for Composites 30th Technical Conference, East Lansing, MI, Sept. 28–30.

[10] Munoz, V., Perrin, M., Pastor, M. L., Welemane, H., Cantarel, A., and Karama, M., 2013, "Application of Non Destructive Testing to the Detection of Aeronautical Defects in Composite Structures," Nonconventional Technologies Review.

[11] Giurgiutiu, V., 2007, *Structural Health Monitoring: with Piezoelectric Wafer Active Sensors*, Elsevier, New York.

[12] Yuan, F.-G., 2016, *Structural Health Monitoring (SHM) in Aerospace Structures*, Woodhead Publishing, Cambridge, UK.

[13] Rose, J. L., 2014, *Ultrasonic Guided Waves in Solid Media*, Cambridge University Press, Cambridge, UK.

[14] Sohn, H., Dutta, D., Yang, J., DeSimio, M., Olson, S., and Swenson, E., 2011, "Automated Detection of Delamination and Disbond From Wavefield Images Obtained Using a Scanning Laser Vibrometer," Smart Mater. Struct., **20**(4), p. 045017.

[15] Park, H. W., Sohn, H., Law, K. H., and Farrar, C. R., 2007, "Time Reversal Active Sensing for Health Monitoring of a Composite Plate," J. Sound Vib., **302**(1–2), pp. 50–66.

[16] Purekar, A., and Pines, D., 2010, "Damage Detection in Thin Composite Laminates Using Piezoelectric Phased Sensor Arrays and Guided Lamb Wave Interrogation," J. Intell. Mater. Syst. Struct., **21**(10), pp. 995–1010.

[17] Rogge, M. D., and Leckey, C. A., 2013, "Characterization of Impact Damage in Composite Laminates Using Guided Wavefield Imaging and Local Wavenumber Domain Analysis," Ultrasonics, **53**(7), pp. 1217–1226.

[18] Hall, J. S., and Michaels, J. E., 2015, "Multipath Ultrasonic Guided Wave Imaging in Complex Structures," Struct. Health Monit., **14**(4), pp. 345–358.

[19] Sohn, H., Dutta, D., Yang, J.-Y., Park, H.-J., DeSimio, M., Olson, S., and Swenson, E., 2011, "Delamination Detection in Composites Through Guided Wave Field Image Processing," Compos. Sci. Technol., **71**(9), pp. 1250–1256.

[20] Tian, Z., Yu, L., and Leckey, C., 2015, "Delamination Detection and Quantification on Laminated Composite Structures With Lamb Waves and Wavenumber Analysis," J. Intell. Mater. Syst. Struct., **26**(13), pp. 1723–1738.

[21] Staszewski, W., Lee, B., and Traynor, R., 2007, "Fatigue Crack Detection in Metallic Structures With Lamb Waves and 3D Laser Vibrometry," Meas. Sci. Technol., **18**(3), pp. 727–739.

[22] Michaels, T. E., Michaels, J. E., and Ruzzene, M., 2011, "Frequency–Wavenumber Domain Analysis of Guided Wavefields," Ultrasonics, **51**(4), pp. 452–466.

[23] Yu, L., and Tian, Z., 2013, "Lamb Wave Structural Health Monitoring Using a Hybrid PZT-Laser Vibrometer Approach," Struct. Health Monit., **12**(5–6), pp. 469–483.

[24] Kudela, P., Radzieński, M., and Ostachowicz, W., 2015, "Identification of Cracks in Thin-Walled Structures by Means of Wavenumber Filtering," Mech. Syst. Sig. Process., **50–51**, pp. 456–466.

[25] Flynn, E. B., Chong, S. Y., Jarmer, G. J., and Lee, J.-R., 2013, "Structural Imaging Through Local Wavenumber Estimation of Guided Waves," Ndt & E Int., **59**, pp. 1–10.

[26] Ma, Z., and Yu, L., 2020, "Ultrasonic Lamb Wave Inspection of Composite Defects," Proc. SPIE 11381, Health Monitoring of Structural and Biological Systems XIV, Online, April 27–May 1.

[27] Tian, Z., Yu, L., Leckey, C., and Seebo, J., 2015, "Guided Wave Imaging for Detection and Evaluation of Impact-Induced Delamination in Composites," Smart Mater. Struct., **24**(10), p. 105019.

[28] Mesnil, O., Leckey, C. A., and Ruzzene, M., 2015, "Instantaneous and Local Wavenumber Estimations for Damage Quantification in Composites," Struct. Health Monit., **14**(3), pp. 193–204.

[29] Ostachowicz, W., Radzieński, M., and Kudela, P., 2014, "50th Anniversary Article: Comparison Studies of Full Wavefield Signal Processing for Crack Detection," Strain, **50**(4), pp. 275–291.

[30] Juarez, P. D., and Leckey, C. A., 2015, "Multi-frequency Local Wavenumber Analysis and Ply Correlation of Delamination Damage," Ultrasonics, **62**, pp. 56–65.

[31] Yu, L., Tian, Z., Li, X., Zhu, R., and Huang, G., 2019, "Core–Skin Debonding Detection in Honeycomb Sandwich Structures Through Guided Wave Wavefield Analysis," J. Intell. Mater. Syst. Struct., **30**(9), pp. 1306–1317.

[32] Ruzzene, M., 2007, "Frequency-wavenumber Domain Filtering for Improved Damage Visualization," *Ultrasonic And Advanced Methods For Nondestructive Testing And Material Characterization.* World Scientific, Singapore, pp. 591–611.

[33] Yu, L., Tian, Z., and Leckey, C. A., 2015, "Crack Imaging and Quantification in Aluminum Plates With Guided Wave Wavenumber Analysis Methods," Ultrasonics, **62**, pp. 203–212.

[34] Tian, Z., and Yu, L., 2014, "Lamb Wave Frequency–Wavenumber Analysis and Decomposition," J. Intell. Mater. Syst. Struct., **25**(9), pp. 1107–1123.

[35] Michaels, J. E., 2017, "Ultrasonic Wavefield Imaging: Research Tool or Emerging NDE Method?" 43rd Annual Review of Progress in Quantitative Nondestructive Evaluation, Atlanta, GA, July 17–22, p. 020001.

[36] Giurgiutiu, V., 2005, "Tuned Lamb Wave Excitation and Detection With Piezoelectric Wafer Active Sensors for Structural Health Monitoring," J. Intell. Mater. Syst. Struct., **16**(4), pp. 291–305.

[37] Yu, L., and Giurgiutiu, V., 2008, "In Situ 2-D Piezoelectric Wafer Active Sensors Arrays for Guided Wave Damage Detection," Ultrasonics, **48**(2), pp. 117–134.

[38] Leong, W., Staszewski, W., Lee, B., and Scarpa, F., 2005, "Structural Health Monitoring Using Scanning Laser Vibrometry: III. Lamb Waves for Fatigue Crack Detection," Smart Mater. Struct., **14**(6), pp. 1387–1395.

[39] Ruzzene, M., Jeong, S., Michaels, T., Michaels, J., and Mi, B., "Simulation and Measurement of Ultrasonic Waves in Elastic Plates Using Laser Vibrometry," AIP Conference Proceedings, AIP, pp. 172–179.

[40] Stepanishen, P. R., and Benjamin, K. C., 1982, "Forward and Backward Projection of Acoustic Fields Using FFT Methods," J. Acoust. Soc. Am., **71**(4), pp. 803–812.

[41] Tian, Z., Howden, S., Ma, Z., Xiao, W., and Yu, L., 2019, "Pulsed Laser-Scanning Laser Doppler Vibrometer (PL-SLDV) Phased Arrays for Damage Detection in Aluminum Plates," Mech. Syst. Sig. Process., **121**, pp. 158–170.

[42] Li, S., Xu, J., and Tang, J., 2018, "Tunable Modulation of Refracted Lamb Wave Front Facilitated by Adaptive Elastic Metasurfaces," Appl. Phys. Lett., **112**(2), p. 021903.

[43] Tian, Z., and Yu, L., 2017, "Wavefront Modulation and Controlling for Lamb Waves Using Surface Bonded Slice Lenses," J. Appl. Phys., **122**(23), p. 234902.

[44] Ma, Z., and Yu, L., 2020, "Laser Based Remote and Rapid Inspection for Composite Plates," Proc. SPIE 11382, Smart Structures and NDE for Industry 4.0, Smart Cities, and Energy Systems, Online, Apr. 27–May 1, p. 113820H.